Journal of Oceanography, Vol. 62, pp. 115 to 132, 2006

Interannual SST Variability in the Japan/East Sea and Relationship with Environmental Variables

SUNGHYEA PARK* and PETER C. CHU

Department of Oceanography, Naval Postgraduate School, Monterey, CA93943, U.S.A.

(Received 28 January 2005; in revised form 3 November 2005; accepted 7 November 2005)

Interannual variability of the Japan/East Sea (JES) sea surface temperature (SST) is investigated from the reconstructed NOAA/AVHRR Oceans Pathfinder best SST data (1985~2002) using the complex empirical function (CEOF) analysis. The iterative empirical function analysis is used for the SST data reconstruction. The first two leading CEOFs account for 86.0% of total variance with 66.4% for the first mode and 19.6% for the second mode. The first CEOF mode represents a standing oscillation and a maximum belt in the central JES. There are two near-7-year events and one 2~3-year event during the period of 1985~2002. The first mode oscillates by adjacent atmospheric systems such as the Aleutian Low, the North Pacific High, the Siberian High, and the East Asian jet stream. Positive correlation in a zonal belt between the first mode JES SST anomaly and the background surface air temperature/SST anomaly reveals intensive ocean-atmosphere interaction near the Polar Front in the North Pacific. The second CEOF mode represents two features: standing oscillation and propagating signal. The standing oscillation occurs in the northern (north of 44°N) and southern (south of 39°N and west of 136°E) JES with around 180° phase difference. A weak southwestward propagating signal is detected between the two regions. The eastward propagating signal is detected from the East Korean Bay to near 135°E. The second mode contains 4~5-year periodicity before 1998 and 2~3-year periodicity thereafter. It is associated with the Arctic Oscillation, which leads it by 1~5-year. Furthermore, a strong correlation with the background surface air temperature/SST anomaly is detected in the tropical to subtropical western Pacific.

Keywords:
- Japan Sea,
- complex empirical orthogonal function,
- interannual variability,
- sea surface temperature anomaly propagation.

1. Introduction

The Japan Sea, known as the East Sea in Korea, with steep bottom topography (Fig. 1) is a unique, semi-enclosed ocean basin. The Japan/East Sea[§], hereafter referred to as JES, covers an area of 10^6 km^2 with a maximum depth in excess of 3,700 m. It is connected with adjacent oceans through only four small (narrow and shallow) straits. It contains three major basins called the Japan Basin (JB), the Ulleung Basin (UB), and the Yamato Basin (YB) and has a high central plateau called the Yamato Rise (YR). It has attracted a great oceanographic interest as a miniature prototype ocean. Its basin-wide circulation pattern, boundary currents, Subpolar Front (SPF), mesoscale eddy activities, and deep water formation are similar to those in a large ocean. JES has large variability, especially in sea surface temperature (SST), produced by a number of environmental forcing at various temporal and spatial scales, such as water exchanges (with surrounding seas), mid-latitude westerlies, atmospheric pressure systems, East Asian monsoon, and climatic forcing from remote regions. Usually JES SST varies on seasonal and non-seasonal (longer than one year) scales. The seasonal variability is connected to the monsoon forcing (Chu *et al*., 1998).

For non-seasonal variability, Chu *et al*. (1998) suggested that JES SST varies with a period of 2~5 years, based on the National Centers for Environmental Prediction (NCEP) monthly SST on a 1° × 1° grid during the period 1981–1994. The connection with the El Niño/Southern Oscillation (ENSO) event was further discussed by Park and Oh (2000) and Hong *et al*. (2001). Minobe *et al*. (2004) identified interannual to interdecadal thermal variability of the JES upper layer (surface to 400 m deep) by analyzing a three-dimensional 0.5° × 0.5° gridded tem-

* Corresponding author. E-mail: spark@nps.edu

§ The Editor-in-Chief does not recommend the usage of the term "East Sea" in place of "Japan Sea".

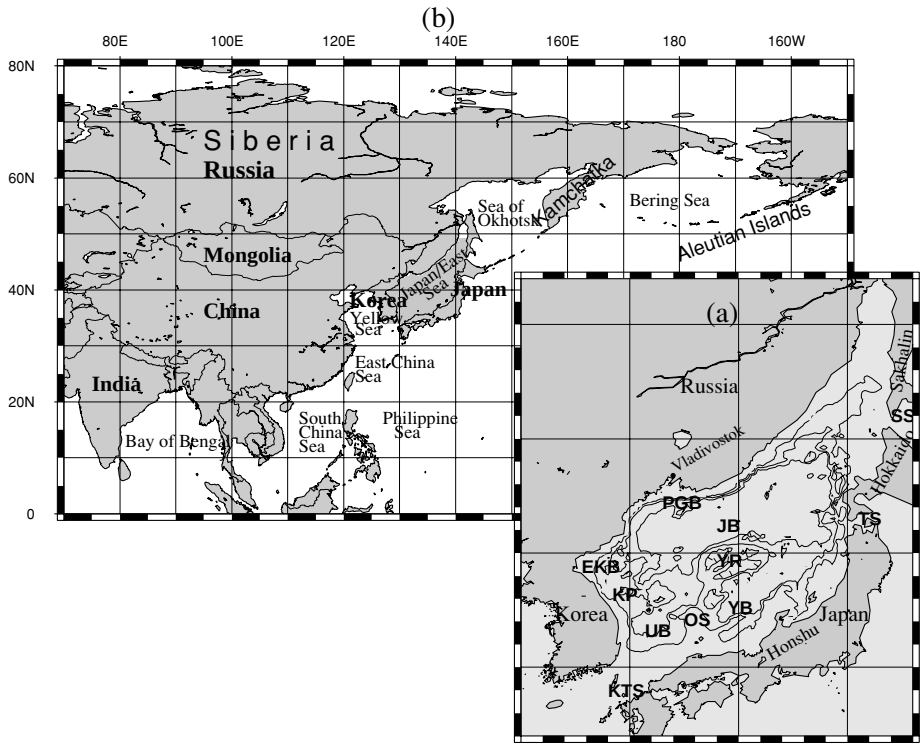

Fig. 1. Geography of the study domain. (a) Japan/East Sea. Contours indicate bottom topography at an interval of 1000 m. Geographical names are as follows: East Korea Bay (EKB), Korea Plateau (KP), Ulleung Basin (UB), Oki Spur (OS), Yamato Basin (YB), Yamato Rise (YR), Japan Basin (JB), Peter the Great Bay (PGB), Korea/Tsushima Strait (KTS), Tsugaru Strait (TS), Soya Strait (SS), and Tartar Strait (TTS). (b) Regional geography.

perature dataset (1957~1996) using complex empirical orthogonal function (CEOF) analysis with a high-pass filter of 7-year cut-off period. However, their study does not include variability with a period of 6~7 years and with horizontal scales smaller than 0.5°. Slow propagation signals in JES related to the interannual variability were detected from satellite data (Park, 1996; Morimoto *et al*., 2000; Hirose and Ostrovskii, 2000), but the cause of the interannual variability has not been discussed.

In this study, the signal propagation and related interannual variability of JES SST are detected from a newly-reconstructed long-term SST dataset with high resolution (finer than 0.5°) using CEOF analysis. The mechanism underlying such variability is obtained from cross-correlation between JES SST and environmental variable anomalies. The remainder of this paper is organized as follows: Section 2 presents retrieval of SST dataset and diagnosis of the newly-reconstructed SST dataset. Section 3 discusses the temporal and spatial characteristics of the interannual variability and its propagation using CEOF analysis. Section 4 shows the relationship of the interannual SST variability to the atmospheric and oceanic variables. Finally, Section 5 presents the conclusions.

2. Data

2.1 Data configurations

NOAA Advanced Very-High-Resolution Radiometer (AVHRR) Oceans Pathfinder global equal-angle best SST data (Version 4.1) are used in constructing a new SST dataset (called the reconstructed SST data) for CEOF analysis. The AVHRR Pathfinder best SST data are considered to be an improvement over previous AVHRR SST data because the cloud detection algorithms, satellite inter-calibration, and quality analysis procedures have been implemented in the AVHRR Pathfinder SST processing. In brief, the configurations of the AVHRR Pathfinder SST data are as follows: 18 km (approximately 0.2° × 0.2°) spatial resolution, 8-day temporal resolution, Hierarchical Data Format (HDF), and 1985~current temporal coverage (Vazquez *et al*., 1998). For the analysis, subset data covering JES (127~142°E and 34~50°N) we extracted from the AVHRR Pathfinder SST data during the period of 1985~2002. The JES subset data comprise 3116 sea-grid points and 824 samples after masking land-grid points. Data acquisition rate in JES is good along the Korean and Russian coasts, but poor east of YR and west of northern Honshu and Hokkaido, where there are over

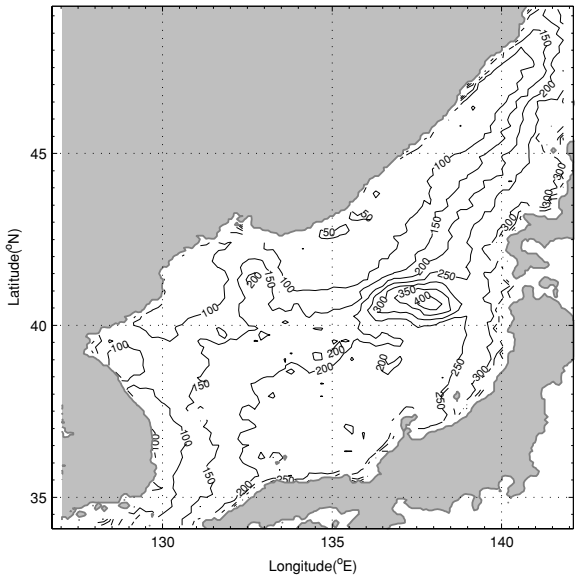

Fig. 2. Distribution of the number of missing records in NOAA/AVHRR Pathfinder best SST achieved through 824 time observations from 1985 to 2002.

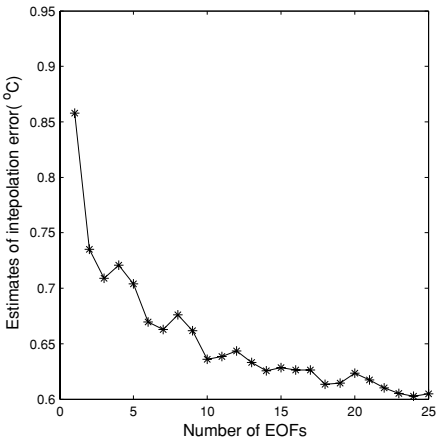

Fig. 3. Estimates of interpolation error measured by 100 validation data. Horizontal axis indicates the number of EOFs retained in the iterative EOF method.

200 interruptions due to missing data (Fig. 2). These missing data should be filled before conducting CEOF analysis.

2.2 Missing data

Malfunction of instruments, cloud coverage, and instrumental errors cause missing data (or bad data). Optimal interpolation has generally been used to fill the missing data the, but this needs *a priori* information about the dataset, such as a decorrelation scale and signal-to-noise ratio. Such information is usually unavailable, however. Instead, an iterative empirical orthogonal function (EOF) method is used in this study. To evaluate the iterative EOF method, a subset of 100 randomly chosen data points (not at missing data points) is used as a validation dataset. During the iterative EOF analysis, the validation data are ignored and treated as the "missing data".

The iterative EOF method is processed as follows. First of all, fill up the missing data (including the validation data) with first-guess values. Compute the first-step EOFs and corresponding principal components using the first-guess values for the missing data. Second, the data at the missing points (including the validation data) are updated using the first-step EOFs and corresponding principal components. The root-mean-square (rms) error,

$$\mathrm{rms} = \sqrt{\frac{\sum_{i=1}^{N}\left(T_i^{\mathrm{int}} - T_i^{ori}\right)^2}{N}}, \quad N = 100,$$

is calculated between the interpolated (T_i^{int}) and original (T_i^{ori}) SST of the validation dataset (called the interpolation error) to evaluate the quality of data interpolation. This process continues until the interpolation (filling) error becomes smaller than a criterion (Beckers and Rixen, 2003). Eight iterations were conducted in this study. The iterative EOF method is able to retain coherent features of the field in interpolating the missing data without *a priori* information about the dataset. The interpolation error decreases with the increasing number of EOF modes. It has a minimum value when the number of EOF modes is 24 (Fig. 3), which shows that the optimal truncation of EOF modes is 24.

Thus, three datasets are available: raw dataset with missing records, interpolated dataset for the missing records (calculated by the iterative EOF method), and the reconstructed dataset which is the combination of the raw and interpolated data. Figure 4 shows the time series of raw, interpolated, and reconstructed data for SST anomaly at 132.2°E and 35.8°N; here the anomaly was obtained by subtracting an annual cycle of SST. When the missing data points are filled using the iterative EOF method, the total variance and variance of the dominant modes (i.e., low modes) increase, whereas the variance of less dominant modes (i.e., high modes) decreases.

2.3 Characteristics of reconstructed SST and SSTA data

SST standard deviation shows high values (>6°C) north of SPF and low values (<6°C) south of SPF with a strong gradient across SPF. Its maximum core (>7°C) is near PGB and central JB, and its minimum core (<5°C) near the Korea/Tsushima Strait (Fig. 5(a)). Such a pattern is caused by differential seasonal forcing. During the summer strong solar radiation penetrates into the entire

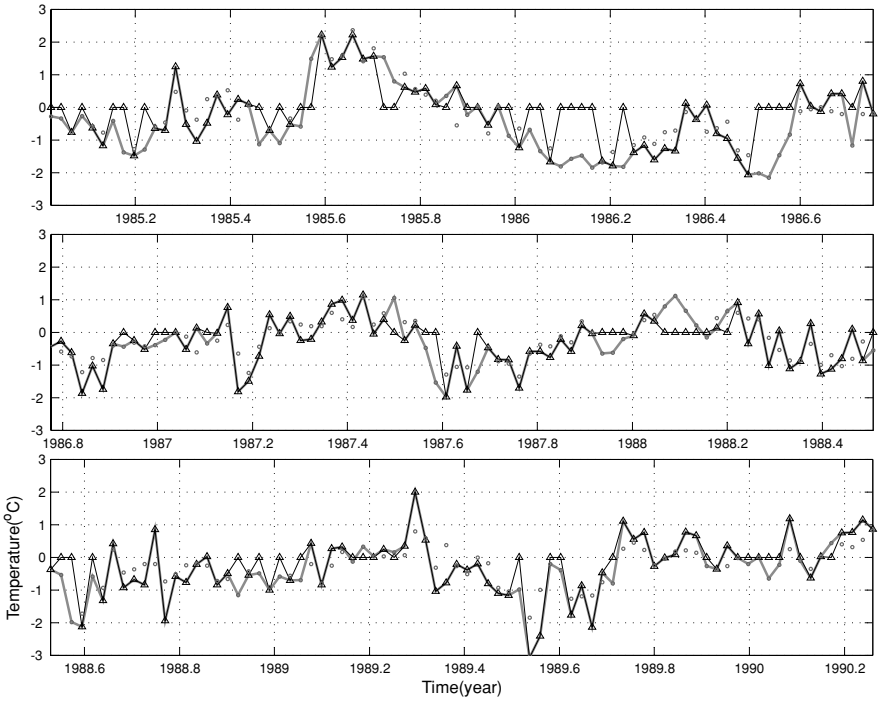

Fig. 4. Descriptions of raw data with missing records (triangle-thin line), interpolated data (open circle), and reconstructed data (thick gray line) at 132.2°E, 35.8°N. The missing records are demonstrated by the fact that temperature, actually sea surface temperature anomaly, is zero in the raw data. The interpolated data are constructed by the iterative EOF method. The reconstructed data are the combination of the raw data for non-missing records and interpolated data for missing records.

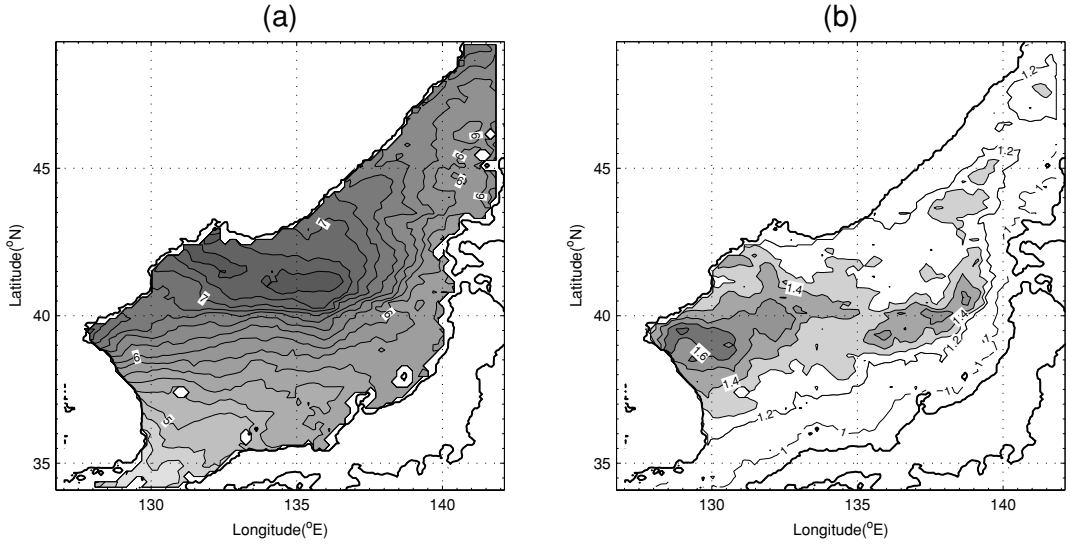

Fig. 5. Standard deviation distributions of SST (a) and SSTA (b), after deleting annual cycle. Contour intervals are 0.2°C and 0.1°C in (a) and (b), respectively.

JES and causes relatively uniform warming, while during the winter atmospheric cooling prevails in the northern JES but is compensated by the warming from the Tsushima Warm Current (TWC) in the southern JES (Park, 1996; Chu *et al*., 2001a, 2001b, 2002).

Since the annual cycle of SST data represents the seasonal variability, SST anomaly (SSTA) is obtained by subtracting the annual cycle (seasonal variability) from the SST data. SSTA standard deviation is much smaller than SST standard deviation, ranging from 1°C along the Japanese coast to 1.6°C near the East Korea Bay (EKB) (Fig. 5(b)). Such an eastward reduction pattern of SSTA standard deviation agrees with Park and Oh's (2000) results on the first EOF mode of filtered SSTA. Moreover, it shows another high core of 1.3~1.6°C west of Honshu and Hokkaido in 39~45°N. This distribution of the high cores implies that the first EOF mode may explain SSTA variability of the central JES, including SPF. A low pass filter with a 400-day moving average is applied to the reconstructed SSTA data to filter out high frequency processes and retain the low frequency processes.

3. CEOF Analysis

3.1 General description

Conventional EOF analysis is able to decompose oceanic/atmospheric signals into spatial and temporal components, but does not allow one to diagnose propagating (or moving) signals (e.g., Chu *et al*., 1997, 1998). The CEOF analysis is an alternative method for detecting propagating signals (Shriver *et al*., 1991).

Decomposition into CEOFs allows one to sort by decreasing variance, revealing spatial structures that propagate in space and vary in time (e.g., Chu and Fang, 2003). We denote temporally varying SSTA data field by $T(x, y, t)$, where (x, y) indicates horizontal position and t is time. We denote complex data field by $\hat{T}(x, y, t)$. The real part of $\hat{T}$ is the original data, T, and the imaginary part is the Hilbert transform of T. The latter is the data field whose phase is advanced in time by $\pi/2$. When the data field $T(x, y, t)$ is expanded into Fourier series,

$$T(x,y,t) = \sum_{\omega} \left[a(x,y,\omega)\cos\omega t + b(x,y,\omega)\sin\omega t \right], \quad (1)$$

then the Hilbert transformation $T_t(x, y, t)$ is represented by

$$T_t(x,y,t) = \sum_{\omega} \left[b(x,y,\omega)\sin\omega t - a(x,y,\omega)\cos\omega t \right]. \quad (2)$$

Thus, the complex data field $\hat{T}(x, y, t)$ is represented by

$$\hat{T}(x,y,t) = T(x,y,t) + iT_t(x,y,t), \quad i \equiv \sqrt{-1}. \quad (3)$$

CEOFs and time series of complex principal/expansion components (PCs) are determined from the covariance matrix derived from the complex time series $\hat{T}(x, y, t)$. CEOFs and PCs are represented by amplitude, as in conventional EOF, and phase, i.e., spatial/temporal amplitude and phase. The covariance matrix of T is Hermitian and positive definite by construction. It has real positive eigenvalues λ_n and corresponding complex eigenvectors $S_n(x, y)$. Hence, the complex data field $\hat{T}(x, y, t)$ is represented by

$$\hat{T}(x,y,t) = \sum_{n} PC_n(t) S_n^*(x,y), \quad (4)$$

where the asterisk signifies the complex conjugate. The spatial function $S_n(x, y)$ and temporal function $PC_n(t)$ are both complex,

$$\begin{aligned} S_n(x,y) &= A_n(x,y)\exp\left[i\theta_n(x,y)\right], \\ PC_n(t) &= B_n(t)\exp\left[i\phi_n(t)\right], \end{aligned} \quad (5)$$

where $[A_n(x, y), \theta_n(x, y)]$ are amplitude and phase for $S_n(x, y)$, and $[B_n(t), \phi_n(t)]$ are amplitude and phase for $PC_n(t)$ (Venegas *et al*., 1998; Venegas, 2001). Each component of $\hat{T}(x, y, t)$,

$$\begin{aligned} \hat{T}_n(x,y,t) &\equiv PC_n(t) S_n^*(x,y) \\ &= A_n(x,y) B_n(t) \exp\left\{ i\left[-\theta_n(x,y) + \phi_n(t) \right] \right\}, \end{aligned} \quad (6)$$

represents a propagating wave pattern (Shriver *et al*., 1991). Given a line of constant phase,

$$\xi_n(x,y,t) \equiv -\theta_n(x,y) + \phi_n(t) = \text{const},$$

we have

$$d\xi_n(x,y,t) = -\left[\frac{\partial \theta_n(x,y)}{\partial x} dx + \frac{\partial \theta_n(x,y)}{\partial y} dy \right] + \frac{\partial \phi_n}{\partial t} dt = 0, \quad (7)$$

or

$$\begin{aligned} k_{nx} &= \frac{\partial \xi_n}{\partial x} = -\frac{\partial \theta_n}{\partial x}, \quad k_{ny} = \frac{\partial \xi_n}{\partial y} = -\frac{\partial \theta_n}{\partial y}, \\ \omega_n &= -\frac{\partial \xi_n}{\partial t} = -\frac{\partial \phi_n}{\partial t}. \end{aligned} \quad (8)$$

The phase speed (c_x, c_y) is calculated by

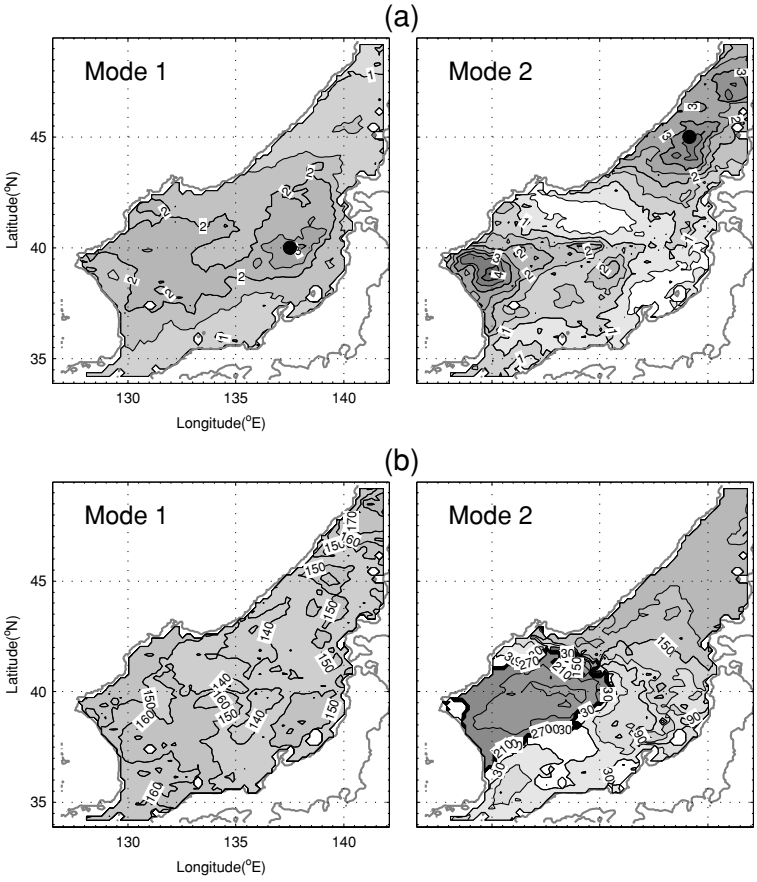

Fig. 6. Spatial amplitude $A_n(x, y)$ distributions (a) and Spatial phase $\theta_n(x, y)$ distributions (b) of each mode. The contour interval of the amplitude is 0.01°C. Signals propagate toward decreasing phase, and contour interval of the phase is 10° (30°) for the first (second) mode.

$$c_{nx} = \frac{\omega_n}{k_{nx}} = \frac{\partial \phi_n / \partial t}{\partial \theta_n / \partial x}, \quad c_{ny} = \frac{\omega_n}{k_{ny}} = \frac{\partial \phi_n / \partial t}{\partial \theta_n / \partial y}. \qquad (9)$$

The direction of the propagating signal is determined by the wavenumber vector (k_{nx}, k_{ny}), or the horizontal variability of the spatial phase $\theta_n(x, y)$. Signal propagation requires the existence of (c_{nx}, c_{ny}), which leads to $k_{nx} \neq 0$, or $k_{ny} \neq 0$, i.e., the spatial phase $\theta_k(x, y)$ is horizontally non-uniform. The temporal phase $\phi_n(t)$ is generally decreased during the period 1985~2002, i.e., $\partial \phi_n / \partial t < 0$ (Fig. 8(b)). As a result, c_{nx}, $c_{ny} > 0$ when $\partial \theta_n / \partial x$, $\partial \theta_n / \partial y < 0$. Thus, the signals propagate toward decreasing phase in the present study.

3.2 Determination of significant CEOF modes

As a prerequisite for interpreting CEOFs it is necessary to determine if the eigenvalues of CEOFs of the SSTA dataset can be distinguished from those produced from a spatially and temporally uncorrelated random process. We evaluated the validity of such eigenvalues at the 95% significance level, assuming as null hypothesis that a dataset is randomly drawn from a population number of uncorrelated Gaussian variables (Overland and Preisendorfer, 1982). Since climate data are generally correlated, their degrees of freedom cannot be the same as they literally are. The reconstructed JES SSTA data are analyzed using the CEOF analysis. At the 95% significance level, the first two leading CEOFs are statistically significant and account for 86.0% of total variance on the time-scale longer than one year, with 66.4% for the first mode and 19.6% for the second mode. Thus, the first two modes are used here to describe the spatial and temporal variability of JES SSTA: the spatial amplitude $A_n(x, y)$, spatial phase $\theta_n(x, y)$, temporal amplitude $B_n(t)$, and temporal phase $\phi_n(t)$.

3.3 Spatial variability

3.3.1 Spatial amplitude

Figure 6(a) shows the spatial amplitudes of the first two modes. Among them, $A_1(x, y)$ has a wide maximum belt in the central JES around SPF and decreases away

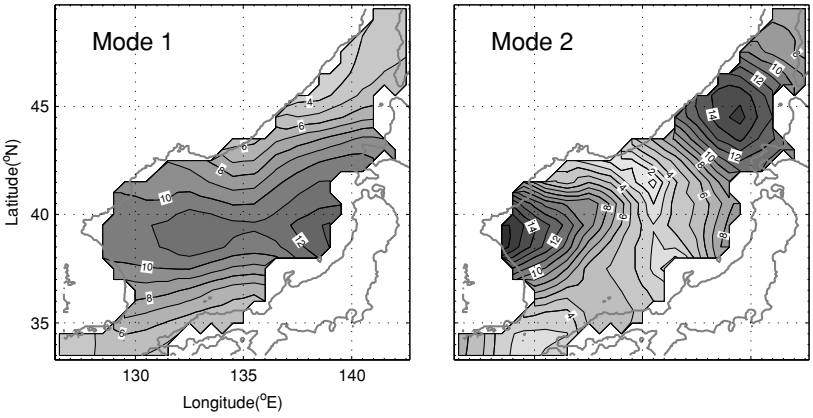

Fig. 7. Spatial amplitude $A_n(x, y)$ distributions using NOAA Optimum Interpolation Sea Surface Temperature dataset with a horizontal grid of 1° × 1° (contour interval is 0.01°C).

from this belt. This pattern resembles the conventional EOF-1 mode calculated by Chu *et al*. (1998). The entire JES has one sign at any instances, according to the conventional EOF-1 mode. The second mode $A_2(x, y)$ shows two high amplitude cores in the southwestern and northeastern JES, and a low amplitude area that is widely extended in the meridional direction, crossing JB and YB. The two high amplitude cores occur as opposite signs in the conventional EOF analysis. This resembles EOF-2 of Chu *et al*. (1998), too.

These distributions of spatial amplitudes using the AVHRR dataset reveal much detail about features that cannot be captured by other widely-used SST datasets. For instance, in the first mode a high amplitude core in closed contours west of Honshu in the AVHRR dataset (Fig. 6(a)) is not clear in spatial amplitudes using the NOAA Optimum Interpolation Sea Surface Temperature dataset (Version 2, referred to as OI dataset), which has been used widely in oceanographic and atmospheric research (Fig. 7); this is a weekly global dataset with a horizontal grid of 1° × 1° and is available at the NOAA-CIRES Climate Diagnostics Center, Boulder, Colorado, USA, from their website at http://www.cdc.noaa.gov. A relatively low amplitude region over YR in the AVHRR data is not detected in the OI dataset. In the second mode a high amplitude region along the Russian coast is composed of two cores, the northern one of which is not shown in OI the dataset.

3.3.2 Spatial phase

Figure 6(b) shows the spatial phases of the first two modes. The spatial phase of the first mode $\theta_1(x, y)$ is quite uniform, which implies a non-propagating signal. The spatial phase of the second mode $\theta_2(x, y)$ has large horizontal variability. The phase $\theta_2(x, y)$ decreases from 180~210° north of 44°N to 0~60° west of 136°E and south of 39°N, showing a phase difference of 150~180° between

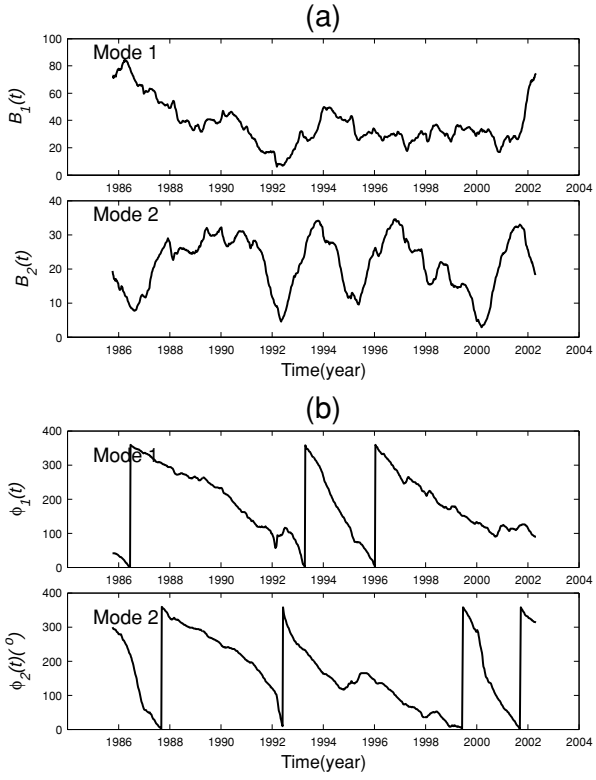

Fig. 8. Temporal amplitude $B_n(t)$ variations (a) and temporal phase $\phi_n(t)$ variations (b) of each mode.

the two regions. This can be interpreted in terms of a signal north of 44°N propagating southwestward while the two regions make a standing oscillation with opposite anomalies. This southwestward propagation, however, is thought to be weak because the spatial amplitude is low between the two regions. Furthermore, the phase $\theta_2(x, y)$

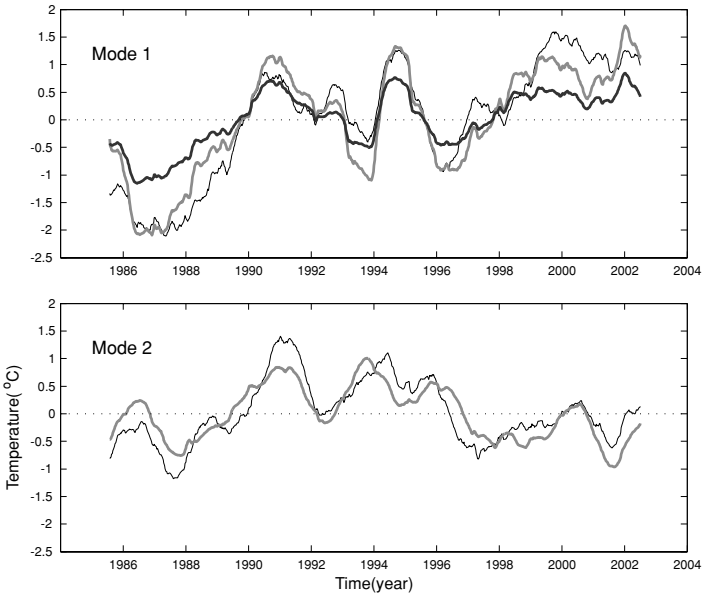

Fig. 9. Temporal variations of the n-th mode SSTA (thick gray line) and SSTA (thin black line) at two locations with the maximum correlation between the n-th mode SSTA and SSTA, denoted by circles in Fig. 6(a): 135.0°E, 41.5°N for the first mode; 139.1°E, 45.0°N for the second mode. Thick black line in the panel of the first mode presents temporal variability of spatial average of SSTA over the Japan/East Sea.

has large horizontal variability in the southwestern JES (around SPF and west of 135°E), indicating an eastward propagating signal of the second mode in the East Korea Bay (EKB) that does not reach 135°E.

3.4 Temporal variability

3.4.1 Temporal amplitude

Temporal amplitudes, $B_1(t)$, $B_2(t)$, represent the intensity of the temporal variability of the first two modes (Fig. 8(a)). The temporal amplitude of the first mode $B_1(t)$ decreases from a maximum to a minimum in 1992, then increases in 1994. After 1995, $B_1(t)$ maintains moderate values. The temporal amplitude of the second mode $B_2(t)$ oscillates and four strong events occur in 1987~1991, 1993~1994, 1996~1997, and 2001, while four quiescent periods occur in 1986, 1992, 1995, and 2000. In particular, a long-lasting strong event occurs from mid-1987 to mid-1991.

3.4.2 Temporal phase

Temporal phases, $\phi_1(t)$, $\phi_2(t)$, represent the periodicity of the temporal variability of the first two modes. A monotonic increase/decrease of the temporal phase $\phi_n(t)$ from 0° to 360° over any 360° interval is inferred as the existence of a certain periodicity in the data (Venegas *et al.*, 1998). In this study, the temporal phase $\phi_n(t)$ decreases with respect to time in all CEOF modes (Fig. 8(b)).

The temporal phase of the first mode $\phi_1(t)$ shows two near-7-year events (1986~1993 and 1996~2002 or so) and one 2~3-year event (1993~1995). This near-7-year periodicity seems to be consonant with earlier results, such as a period of 5~7 years in the dominant spectral energy density of JES SSTA during the period 1951~1996 (Park and Oh, 2000), and a period of 7 years in CEOF-1 of the northwestern Pacific SSTA (1945~1989) including JES (Trousenkov *et al.*, 2001), regardless of their slightly-different temporal and spatial coverage. On the other hand, this near-7-year periodicity is not found in Minobe *et al.* (2004) due to a cut-off period of 7 years. The 2~3-year event (1993~1995) includes record-breaking cold and hot summers in 1993 and 1994, respectively (Yoo *et al.*, 2004), the amplitude of which cannot be negligible.

The dominant periodicities of $\phi_2(t)$ is estimated at 4~5 years before 1998 and at 2~3 years thereafter. Shortening of the temporal variability in the 1990s has also been discussed in earlier studies (Chu *et al.*, 1998; Hirose and Ostrovskii, 2000; Morimoto and Yanagi, 2001; Minobe *et al.*, 2004). This phenomenon seems to coincide with 1998/1999 changes over the North Pacific (Minobe, 2002).

3.4.3 Temporal variability at maximum correlation between SSTA and CEOF modes

Consider the real parts of $\hat{T}(x, y, t)$ (see Eq. (4)) and $\hat{T}_n(x, y, t)$ (see Eq. (6)): $T(x, y, t)$ and $T_n(x, y, t)$. Here, $T_n(x, y, t)$ denotes the n-th mode SSTA at each grid point. Correlation coefficients were calculated between $T(x, y, t)$ and $T_n(x, y, t)$ at the grid point (x, y). The location of

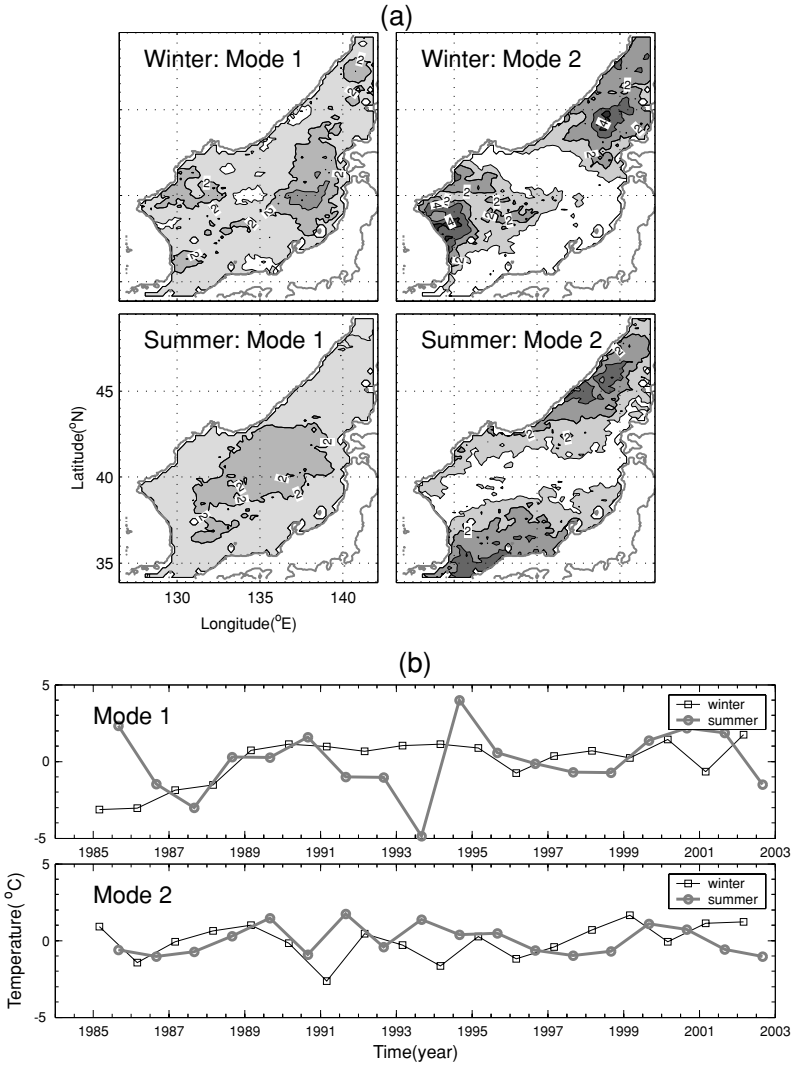

Fig. 10. Seasonal CEOF. (a) Spatial amplitude (contour interval is 0.01°C), and (b) temporal variation at the grid with a maximum spatial amplitude: (137.5°E, 39.7°N) for the winter first mode, (134.3°E, 41.5°N) for the summer first mode, (128.8°E, 39.4°N) for the winter second mode, and (139.9°E, 46.3°N) for the summer second mode.

the maximum correlation (x_{max}, y_{max}) is marked as a solid circle in Fig. 6(a). The n-th mode of SSTA $T_n(x, y, t)$ at (x_{max}, y_{max}) can be regarded as representative of temporal variability of the n-th mode, $T_n(x_{max}, y_{max}, t)$, and can describe the occurrences of warm and cold events. The maximum correlation coefficient is 0.93 and 0.84 for the first and second modes, respectively.

Temporal variability shows that the first mode SSTA (i.e., $T_1(x_{max}, y_{max}, t)$) fits SSTA (i.e., $T(x_{max}, y_{max}, t)$) quite well (Fig. 9). Resemblance between first mode SSTA and spatial-mean SSTA indicates that the first mode SSTA represents the spatial-mean SSTA to a great extent. Three cold events (1986~1988, 1993, and 1996) and three warm events (1990~1991, 1994, and 1998~2002) can be identified either from the spatial-mean SSTA or the first mode SSTA. Once the anomalies are generated, they are sustained over one year and sometimes over two years, such as 1986~1987 and mid-1998~mid-2000. In particular, positive anomalies lasting in 1999 become weak after 2000 and then strong again in 2002; negative anomalies, which are expected to occur subsequently, are not found. This warming trend of JES is supposed to be a local demonstration associated with recent global warming since the late 1990s (McPhaden, 2002; Minobe, 2002; Schwing *et al.*, 2002; CLIVAR, 2003; Oelke *et al.*, 2004).

The second mode SSTA $T_2(x_{max}, y_{max}, t)$ resembles SSTA $T(x_{max}, y_{max}, t)$. It shows five warm events occurring in 1986, 1990~1991, 1993~1994, 1996, and 2000 and

five cold events occurring in 1987~1988, 1992, 1997~1999, and 2001~2002. The cold events are relatively long and the warm event is relatively short after 1997. A difference is found between the first and second SSTA modes. The first SSTA mode shows a warm event only after 1998, but the second SSTA mode shows both warm and cold events.

3.5 Seasonal CEOF

As mentioned in Subsection 2.3, the standard deviation of JES SST shows that JES is influenced by differential seasonal forcings. That provides a possibility that the differential seasonal forcings on JES might produce differential seasonal CEOF modes. If so, we should study the following problems: How is the seasonal (summer and winter) CEOF different from the non-seasonal CEOF using all-season data? Which season is more influential in the interannual variability of JES SSTA of the all-seasons data?

CEOF is used to analyze February (winter) and August (summer) SSTA time series. Summer total variance is about double the winter one. The first two leading winter (summer) CEOFs account for 67.9% (89.3%) of total variance with 47.3% (81.8%) for the first mode and 20.6% (7.5%) for the second mode. The summer first mode shows that a high amplitude core distributes evenly in the central JES (Fig. 10(a)). This summer pattern is attributed to warming over the entire JES, which overwhelms temperature changes due to currents that may not be spatially uniform. On the other hand, the winter first mode shows a high amplitude core west of Honshu and Hokkaido, rather than the central zonal belt. This is attributable to the Japanese Coastal Branch, referred as the Nearshore Branch in Japanese literature, which is a branch of the Tsushima Warm Current and flows along the Japanese coast starting from the eastern channel of the Korea/Tsushima Strait. Its variability seems to influence wintertime SSTA variability west of Honshu and Hokkaido. It is considered to be relatively permanent throughout the seasons (Hase *et al.*, 1999), and its wintertime influence on SSTA is rather more dominant than in other seasons. The winter second mode resembles the non-seasonal one, while the summer second mode is very different from the non-seasonal one. It is hard to detect propagation signals in the spatial and temporal phases due to poor temporal resolution of the time series. It is possibly hard to address exact periodicity in each mode (Fig. 10(b)). Nonetheless, temporal variation of the summer first mode SSTA at the grid point with a maximum in spatial amplitude resembles the non-seasonal one. Both second modes also show the interannual variability of 2~5 years. The winter first mode SSTA reveals a strong cooling event before 1989 and then sustains a mild warming event for 7 years (1989~1995). The distinguished event in 1993~1994 is not detected in the winter first mode SSTA. The winter second mode SSTA shows greater interannual variability than the summer one. The summer first (winter second) mode is therefore more influential on the non-seasonal first (second) mode than the winter (summer) one. It is noted that the high amplitude core of the first winter mode exists in the non-seasonal one.

3.6 Propagation of second mode SSTA

Figure 11 shows temporal variation of the second mode SSTA $T_2(x, y, t)$ from mid-1987 to mid-1993. Fractional years are used, e.g., 1987.5 indicates mid-1987. The temporal phase $\phi_2(t)$ changes from 1° in 1987.7 to 55° in 1992.3. The duration of phase change of 360° denotes the whole period of the dominant cycle. A cycle with a period of around 4.5 years can be identified from 1987.7 to 1992.4.

At $\phi_2 = 1°$ (i.e., 361°), a warm (cold) anomaly is detected in the southwestern (northeastern) JES. As the phase decreases, a warm anomaly core near EKB spreads eastward, and the cold anomaly propagates southwestward over the southeastern extrusion region of JB, reaching west of 136°E at $\phi_2(t) = 300°$. The eastward propagating speed of this warm anomaly core near EKB is estimated as 0.02~0.03 m/s in time-distance plot (not shown). Minobe *et al.* (2004) described a weak northward and northeastward propagation from the Korea/Tsushima Strait to 135°E and 40°N on a timescale of interannual variability. According to a rough approximation on the basis of phase difference and the period of interannual variability, its propagation is compatible with the present result.

At $\phi_2(t) = 280°$ a new warm anomaly is intensified west of Hokkaido, expands to the south and to the north, and then makes two warm anomaly cores at $\phi_2(t) = 243°$ (as shown as two cores in the northern amplitude maximum in Fig. 6(a)). At the same time the cold anomaly (west of 136°E and south of 39°N) propagating from the northeast begins to mature. The phase $\phi_2(t)$ decreases slowly with time after $\phi_2(t) < 280°$. At $\phi_2(t) = 221°$ a new cold anomaly emerges in EKB and matures. The second mode $T_2(x, y, t)$ has a totally opposite structure between $\phi_2(t) = 179°$ and $\phi_2(t) = 1°$. The phase $\phi_2(t)$ decreases quickly with time after $\phi_2(t) < 179°$. Eventually, a warm (cold) anomaly covers the southwestern (northeastern) JES at $\phi_2(t) = 55°$ and 331°. The speed of the southwestward propagating signal is estimated as ~0.01 m/s (Fig. 6(b)): the phase difference between north of 44°N and west of 136°E and south of 39°N is 150~180°, the distance between the two is 600~1000 km, and the period is roughly 4 years (though the dominant periods of the second mode are 2~3 years and 4~5 years). Morimoto *et al.* (2000) reported that warm and cold eddies in YB and YR move southwestward with a speed of 0.01 m/s, based on

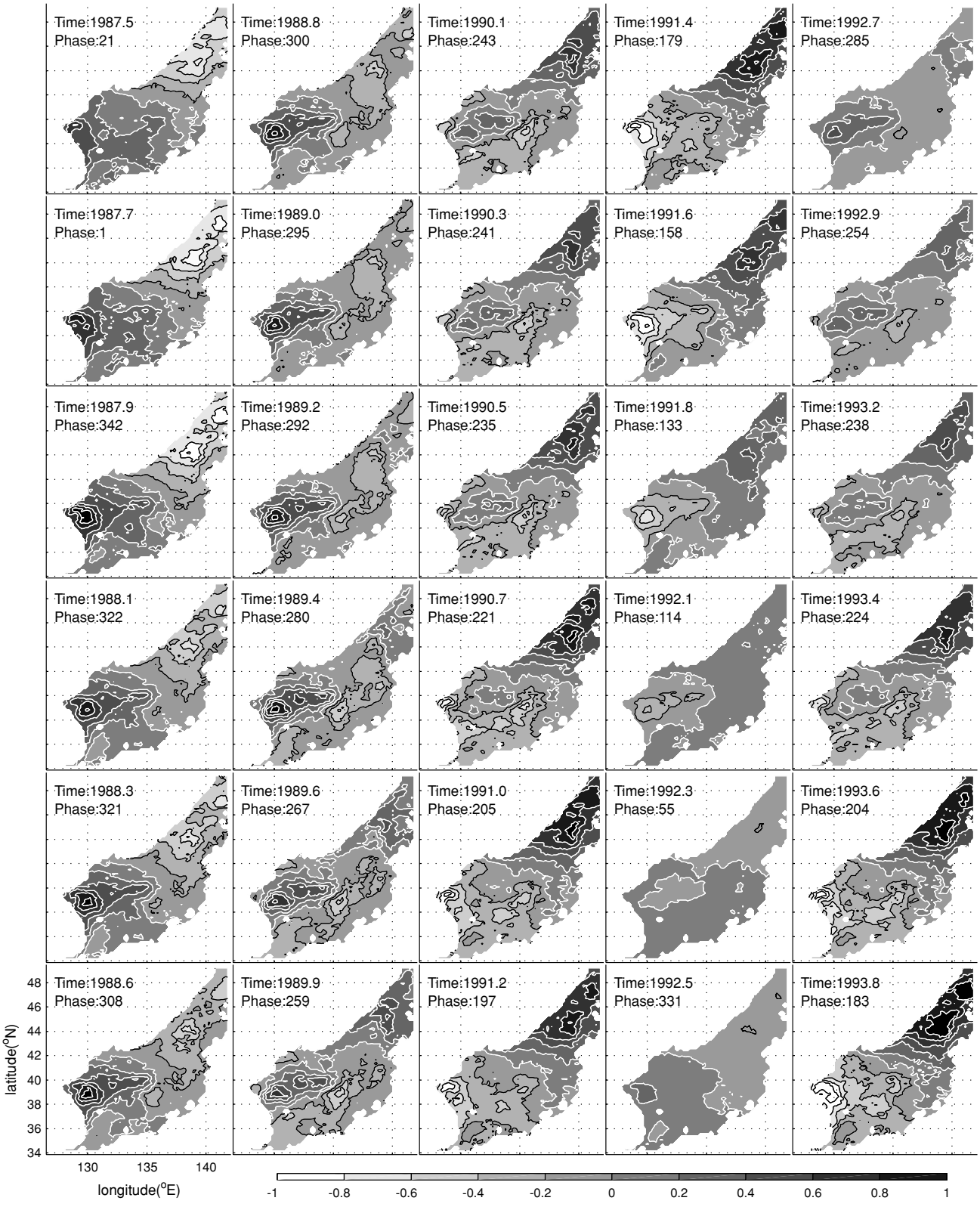

Fig. 11. Evolutions of the second mode SSTA over mid-1987~mid-1993 with an interval of 80 days. Phase changes from 360° to 0°. Time instance is recorded as the fraction of a year; e.g., the fraction 1987.5 indicates mid-1987. Contour interval is 0.2°C. Black (white) contours indicate negative (zero and positive) anomaly.

a lag correlation analysis of TOPEX/POSEIDON-ERS SSHA data. Since the lifetime of an eddy in JES is less than 1 year according to their study, it is difficult to conclude that this southwestward propagating signal corresponds exactly to the propagation of those eddies. However, our result evidently shows at least the existence of the southwestward propagating signal from the northeastern JES to the southwestern JES.

4. Relationship to Environmental Variables

Earlier studies have shown the connection of JES SSTA variability (sometimes northwestern Pacific SSTA including JES) to the northwestern Pacific sea level pressure (especially Aleutian Low), ENSO event, East Asian jet stream, East Asian monsoon, Siberian High, and Arctic Oscillation (Ponomarev *et al*., 1999; Lau *et al*., 2000; Park and Oh, 2000; Hong *et al*., 2001; Trousenkov *et al*., 2001; Minobe *et al*., 2004). These phenomena are interrelated (Wang *et al*., 2000; Gong *et al*., 2001; Wu and Wang, 2002; Lin *et al*., 2002; Gong and Ho, 2003). Therefore, we examine the relationship of JES SSTA variability to the environmental variables representing these phenomena. Consider a wider region (70°E~150°W, 0~80°N) covering the western Pacific Ocean, the Asian continent, and a part of the northern Indian Ocean (called the background region). We analyze sea level pressure (SLP), surface air temperature (SAT), SST, and four climate indices such as the Arctic Oscillation Index (AOI), North Pacific Index (NPI), Western Pacific Pattern Index (WPI), and Multivariate ENSO Index (MEI).

4.1 Configurations of environmental variables

SLP and SAT datasets are obtained from the Climate Diagnostics Center derived NCEP Reanalysis Products with monthly interval and 2.5° × 2.5° spatial resolution (available at http://www.cdc.noaa.gov/). The SST dataset was mentioned above in Subsection 3.3.1. AOI (Thompson and Wallace, 1998) is characterized by SLP anomalies of one sign in the Arctic and opposite sign centered about 37~45°N. The interannual and longer-term changes in the wintertime Arctic Oscillation have an enormous impact on the climate of the northern hemisphere (Thompson and Wallace, 2001; available at http://tao.atmos.washington.edu or www.cpc.ncep.noaa.gov). NPI is an area-weighted SLP over the region of 160°E~140°W and 30~65°N. It is a good index of the intensity of the Aleutian Low (Trenberth and Hurrell, 1994) as well as an indicator of major climate processes in the North Pacific (available at http://www.cgd.ucar.edu/~jhurrell/np.html). WPI represents a primary mode of low-frequency variability over the North Pacific in all months (Barnston and Livezey, 1987; available at http://ingrid.ldgo.columbia.edu). MEI is an average of the main ENSO features contained in the following six observed variables over the tropical Pacific: SLP, the east-west and north-south components of the surface wind, SST, SAT, and total amount of cloudiness (available at http://www.cdc.noaa.gov/ENSO). Positive values of the MEI represent the warm ENSO phase (Wolter and Timlin, 1993, 1998).

All the data were prepared over the common period, 1985~2002, after removing the annual cycle and applying a 13-month moving average. We now call them the background anomaly data (SLPA, SATA, and SSTA). The JES SSTA variability of the n-th mode, i.e., the n-th mode SSTA, is represented by $T_n(x, y, t)$ at the grid $(x_{\max}, y_{\max})$ where correlation coefficients between $T(x, y, t)$ and $T_n(x, y, t)$ are at a maximum, as described in Subsection 3.4.3. The n-th mode SSTA is re-sampled in monthly interval to match its temporal resolution to the corresponding environment variables.

4.2 Correlation analysis

Lagged correlation coefficient (LCC) was used to investigate relationship between two variables. Let $[X(t), T(t)]$ be the time series of the environment variables and the n-th mode SSTA, respectively, which are normalized by their standard deviations. The lagged correlation coefficients are calculated between two normalized time series. The negative lag in the following figures indicates that the environment variables lead the n-th mode SSTA.

Since the (lagged) correlation coefficient measures the strength of a linear relationship, we need to examine whether a relationship exits between $X(t)$ and $T(t)$. This is done using scatter diagrams between the two normalized time series (Wilks, 1995). Most of the scatter diagrams reveal a robust or at least moderate linear relationship (not shown). Hence, the relationship of JES SSTA variability to the environment variables can be interpreted using the (lagged) correlation coefficient on an assumption of linearity.

4.3 Correlation between n-th mode SSTA and CIs

Figure 12 shows LCCs between the n-th mode SSTA and CIs. The LCC pattern of WPI resembles that of MEI in both modes, confirming the existence of a relationship between them. Indeed, MEI is highly positively correlated to WPI at zero lag and seems to lead WPI slightly, by 1~2 months (not shown). The LCC patterns of AOI and NPI are similar in the first mode but less so in the second mode. In the first mode the LCC of NPI (or AOI) is out of phase to that of WPI (or MEI) as a correlation between CIs (not shown). This supports the hypothesis that the cold anomaly of the northwestern Pacific SST is related to the negative phase of AOI, low SLP in the midlatitude, and warm ENSO event (Thompson and Wallace, 1998; Wang *et al*., 1999). The first mode SSTA is positively correlated to NPI and AOI and negatively

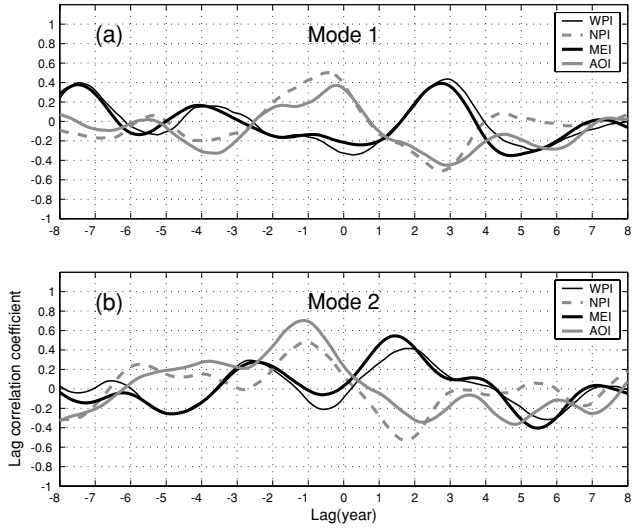

Fig. 12. Lag correlation coefficients between the climate indices and the *n*-th mode JES SSTA, where negative lag indicates that the climate indices lead JES SSTA. (a) First mode, and (b) second mode.

(weakly) correlated to WPI and MEI at zero lag. NPI shows the highest correlation coefficient of 0.5, which leads the first mode SSTA by 3~6 months. The second mode SSTA is weakly correlated to AOI, almost uncorrelated to the other three CIs at zero lag, but highly correlated to AOI (0.7) and moderately to NPI (>0.4) at around –1 year lag. This lagged correlation implies that the second mode seems to be linked to remote forcing with a long memory compared to the first mode. Such remote forcing is thought to be linked to the change of the surface heat flux (via atmospheric circulation systems), which is one of the key components affecting SST anomalies (Alexander *et al*., 2002). In both modes correlations to MEI and WPI are not as strong as those to AOI and NPI, implying that connection with ENSO might not be the most significant.

4.4 Correlation between n-th mode SSTA and background (SLPA, SATA, SSTA)

When the number of variables is large, geographic arrangement of data locations can be used to organize correlation information in map form. LCCs are calculated between *n*-th mode SSTA and the background fields (SLPA, SATA, and SSTA) at each grid point of the background fields with a certain lag, and evaluated at corresponding grid points. A correlation map not only displays geographical patterns of correlation coefficients but also provides informative teleconnection patterns. In addition, consecutive correlation maps with changing lags show the evolution of such patterns. The correlation map is therefore appropriate to interpret the relationship of one variable (*n*-th mode SSTA) to the others arranged with background fields geographically.

4.4.1 LCC for the first mode SSTA

The background SLPA is related to the first mode SSTA at –12~0-month lag with a dipole pattern (Fig. 13): a positive correlation extends to east of 160°E and south of 60°N, with a negative correlation over the Asian continent, the East China Sea, and the Yellow Sea. The positive correlation seems to be associated with the southern part of the Aleutian Low and the western part of the North Pacific High/Subtropical High, while the negative correlation with the Siberian High. On climatological SLP charts these low and highs reside as follows: the Aleutian Low (130°E~140°W, 40°~60°N), the North Pacific High (160°E~130°W, 20°~40°N), and the Siberian High (70°~120°E, 40°~60°N). They are considered as key regulators of the extratropical climate in the Northern Hemisphere; the Aleutian Low and the Siberian High are especially influential in winter, while the North Pacific High exerts its influence in summer. The dipole pattern suggests that strengthening of the Aleutian Low and the Siberian High triggers a cold anomaly in the first mode SSTA. In winter, in particular, Strengthening of the Aleutian Low and the Siberian High enhance pressure gradient in the zonal direction, resulting in a stronger cold air flow from the Asian continent over JES. Strengthening of the North Pacific High, especially in summer, induces a stronger warm air flow over JES from the subtropics/tropics, which interprets the warm anomaly in the first mode SSTA. Numerous studies emphasize the impacts of summertime variability of the North Pacific High on the East Asia climate.

The background SATA is highly correlated to the first mode SSTA at –12-month to zero lag with the strongest correlation in the central JES exhibiting a similar pattern with spatial amplitude of the first mode SSTA (Fig. 6(a)). Including this strongest correlation core, a zonal belt of high positive correlation coefficients (>0.5) between 30°N and 50°N appears at around –12-month lag, intensifies through –6-month lag to zero lag, and finally weakens at +6-month lag. This belt implies a strong connection to the East Asian jet stream, which is a westerly with a maximum speed in the upper troposphere and covers the Asian continent and the northwestern Pacific, migrating between 20°N and 50°N. Since it affects the surface pressure system and air temperature field over East Asia and the western Pacific at its greatest extent (Yang *et al*., 2002), the zonal winds extend from the surface to the upper troposphere (1000, 850, 500, and 200 hPa). The zonal wind data were also from Climate Diagnostics Center derived NCEP Reanalysis Products with monthly interval and 2.5° × 2.5° spatial resolution over the common period. A time series that can represent the East Asian jet stream is introduced, which is composed of zonal wind velocities

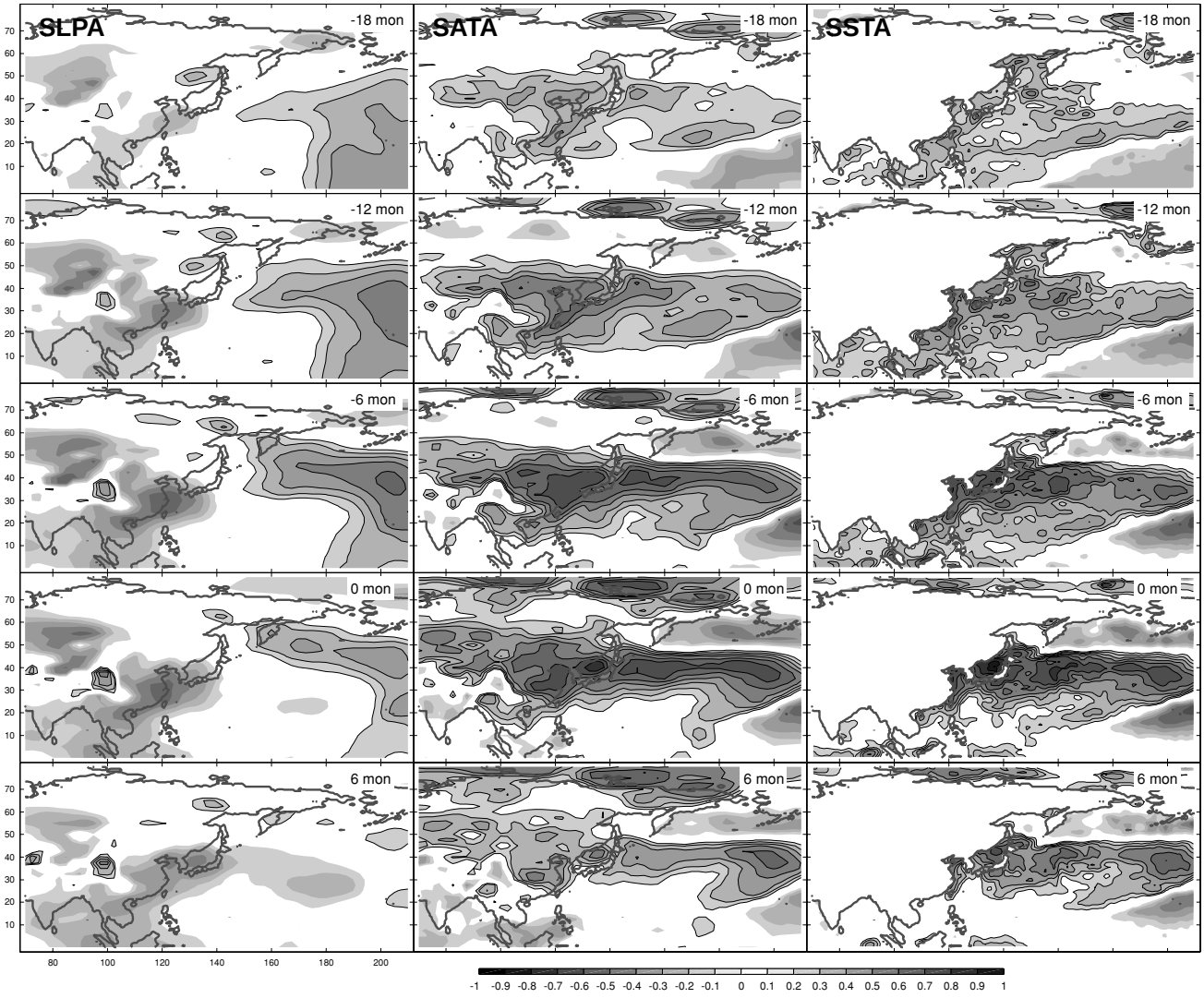

Fig. 13. Lag correlation coefficients between the first mode (JES) SSTA and the background SLPA, SATA, and SSTA, where the negative lag indicates that the background variables lead the first mode (JES) SSTA. Shading represents where absolute values of correlation coefficients are greater than 0.2. Shading interval is 0.1, and shadings with (without) contours indicates positive (negative) correlation. Horizontal and vertical axes are longitude (°E) and latitude (°N), respectively, and 200°E indicates 160°W.

averaged in 100°~180°E and 25°~40°N where a high velocity core is shown in annual-mean zonal wind field at 200 hPa.

LCCs between the zonal wind and the first mode SSTA are calculated at four pressure levels (1000, 850, 500, and 200 hPa; Fig. 14(a)). The zonal wind leads the first mode SSTA by less than 5 months at all four pressure levels. High negative correlations of <–0.6 are shown at 500 hPa and 200 hPa. In the correlation map between the zonal wind and the first mode SSTA (Fig. 14(b), showing the strongest correlation), a high negative correlation zonal belt is shown in 25°~40°N where the East Asian jet stream resides climatologically. These features imply that strong East Asian jet stream is associated with the cold anomaly in the first mode SSTA. Since the strong East Asian jet stream is related to the intensification of atmospheric circulation systems, including the Asian continent high such as the Siberian High, the east Asian trough, the Aleutian Low, and so forth, the east Asian winter monsoon then strengthens (Yang *et al.*, 2002; Jhun and Lee, 2004). JES SST becomes cold in response to the atmospheric forcing. Such a connection is in agreement with the dipole pattern in the background SLPA. In addition, it is consistent with an earlier result that the weak 200 hPa westerly over the subtropical Asia precedes the strong Asian summer monsoon (Yang *et al.*, 2004), although our

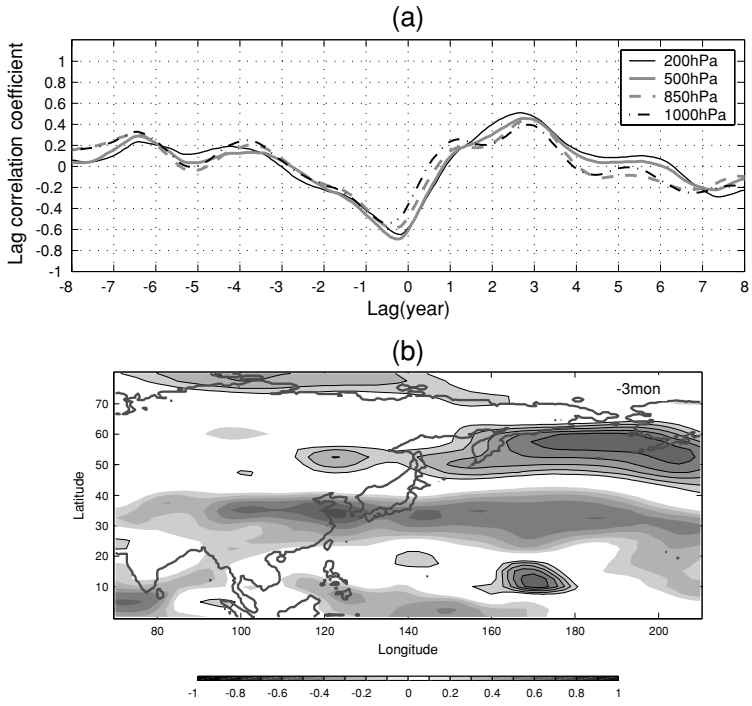

Fig. 14. (a) Lag correlation coefficients between the zonal wind velocities averaged in 100~180°E and 25~40°N (at 1000, 850, 500, 200 hPa) and the first mode (JES) SSTA, where negative lag indicates that the zonal wind lead the first mode SSTA. (b) Lag correlation coefficients between the zonal wind velocities (at 500 hPa) in the background region and the first mode SSTA when the zonal wind leads the first mode SSTA by 3-month. Detail configurations of this figure are as Fig. 13.

understanding of the relationship between variability of the summertime East Asian jet stream and the Asian summer monsoon is incomplete (Lin and Lu, 2005).

A negative correlation is detected over the Bering Sea and the subtropical to tropical central Pacific. The in-phase correlation in these two regions is consistent with Niebauer *et al*. (1999). This correlation distribution might suggest that warm SAT over the Bering Sea and/or the subtropical to tropical central Pacific is accompanied by a cold anomaly of the first mode SSTA.

The first mode SSTA is correlated with neighboring waters at –12-month lag and exhibits a strong positive correlation in the zonal belt extending from 30°N to 50°N at –6-month to zero lag as its LCC distributions with SATA. The positive correlation persists even at +6-month lag because the ocean has a larger heat capacity and slower heat transfer rate than the atmosphere. This positive zonal belt seems to be associated with the Polar Front in the Pacific extending 40°~50°N in mean circulation field. The Polar Front region is considered to be a place where an intensive ocean-atmosphere interaction occurs in winter and where ocean's memory of past wind system changes is reconstructed and affects SST variations (Nonaka and Xie, 2003). For these reasons this region plays a key role in climate regulation in the North Pacific, and the first mode SSTA is strongly connected with it.

4.4.2 LCC for second mode SSTA

The background SLPA is correlated to the second mode SSTA at –18~0-month lag (Fig. 15, not shown at –18-month lag) with high positive LCC in the zonal region between 40°N and 60°N (>0.6) and high negative LCC in the Arctic (60°~80°N). This correlation pattern consists of a positive correlation between AOI and the second mode SSTA (>0.5) at –2~0-year lag (Fig. 12(b)). In contrast, high LCC is detected at positive lags in low latitudes: positive correlation west of 150°E and negative correlation east of 150°E. Such a sign-shift of correlation pattern with increasing phase is considered to be a manifestation of the high latitude variability transferring to the low latitude. Teleconnection of the Arctic Oscillation to the East Asian monsoon has been demonstrated by several studies (Gong *et al*., 2001; Gong and Ho, 2002, 2003; Wu and Wang, 2002). Weak correlation over JES throughout the entire lag suggests that the influence of SLPA over JES in the second mode SSTA is not as strong as that of the Arctic Oscillation.

The second mode SSTA is negatively correlated to the background SATA south of 40°N extending over India, south China, the Bay of Bengal, the Philippine Sea, and the subtropical to tropical western Pacific at –12-

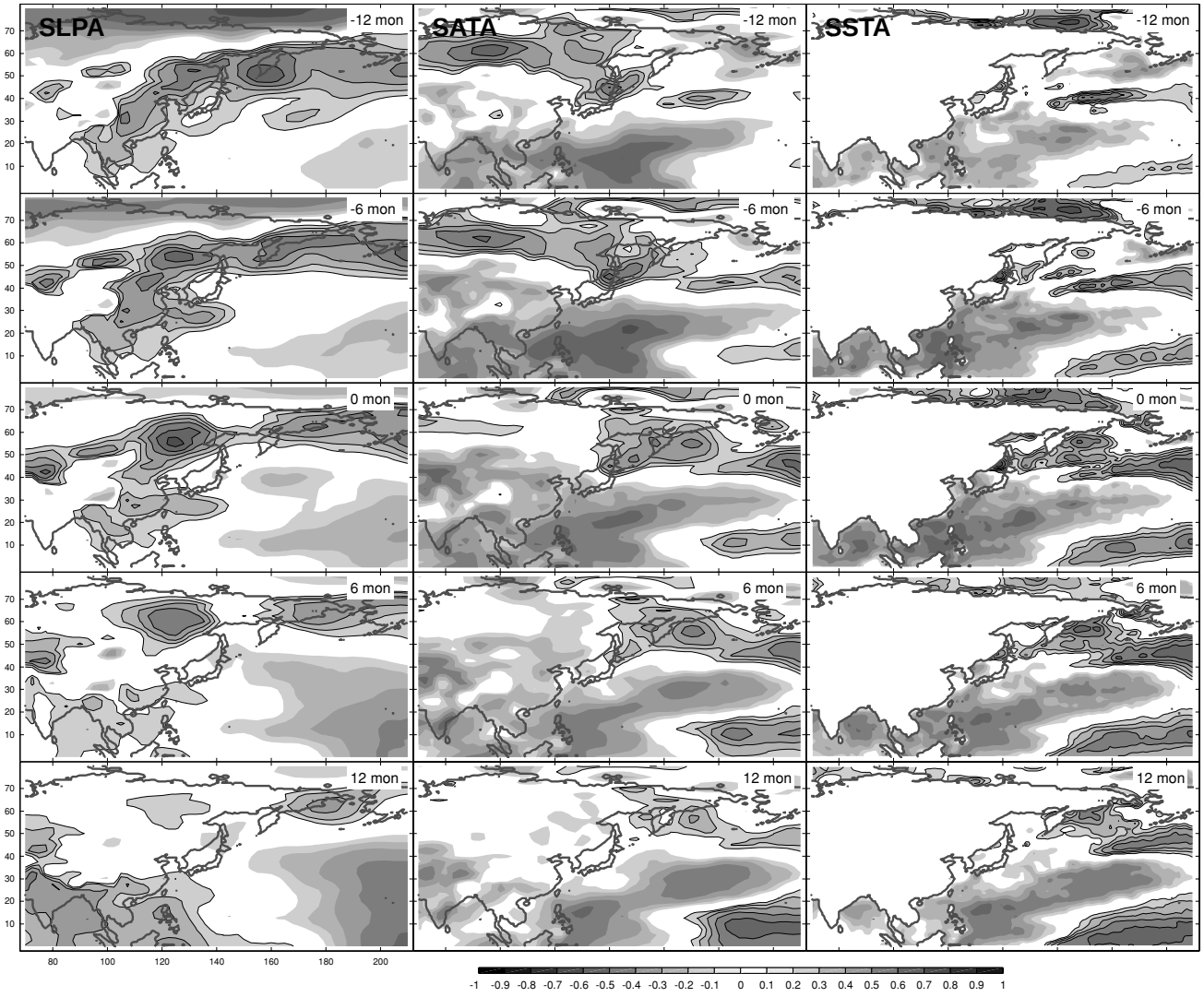

Fig. 15. As Fig. 13 except for the second mode (JES) SSTA.

month to +24-month lag. The strongest negative correlation zone (LCC <–0.6) is located in the Philippine Sea and the western Pacific Ocean between 20°~30°N and propagates eastward as the lag increases. At –12-month to –6-month lag, two positive LCC cores are detected in the northern boundary of the Siberian High and northeastern JES. Since SAT in northern boundary of the Siberian High is subject to the Arctic Oscillation (Wu and Wang, 2002; Gong and Wang, 2003), the Arctic Oscillation can affect the second mode SSTA in the northeastern JES via the northern boundary of Siberian High.

Like the background SATA, a strong negative LCC distributes in the tropical to subtropical western Pacific of the background SSTA. This negative correlation is strongest in 20°~30°N, where the Subtropical Polar Front is located. At –6 month to +12-month lag, the southwestern JES also shows a negative correlation. It implies that cooling (warming) in the Subtropical Gyre is accompanied by cooling (warming) in the second mode of the southwestern (northeastern) JES. Consistently, the negative LCC in the East China Sea protrudes toward JES at –6-month to zero lag.

5. Conclusions

The patterns and causes of interannual variability of JES SST have been investigated using the CEOF analysis of the newly-reconstructed SST dataset (1985~2002) from the NOAA/AVHRR Oceans Pathfinder best SST data by iterative EOF analysis. Subtraction of annual SST fields and 400-day moving-average were performed, and then the reconstructed SSTA dataset was established. The first two leading CEOFs account for 86.0% of total vari-

ance on a time-scale of longer than one year with 66.4% for the first mode and 19.6% for the second mode.

The first CEOF mode has the maximum belt in the central JES around the SPF and decreases away from this belt. The spatial phase is so uniform that the first mode is characterized as a standing oscillation. There are two near-7-year events and one 2~3-year event during the period of 1985~2002. The second mode shows two high amplitude cores in the southwestern and northeastern JES, and the low amplitude area is widely stretched in the meridional direction, crossing JB and YB. The signal detected near EKB propagates eastward with a speed of 0.02~0.03 m/s but does not reach 135°E. The southwestward propagating signal moves from the northern JES (north of 44°N) to the southwestern JES (west of 136°E, south of 39°N) while the two regions make a standing oscillation with opposite signs. It is considered weak, however, because the spatial amplitude is low between the two regions. The dominant periodicities are estimated as 4~5 years before 1998 and at 2~3 years thereafter.

The causes of the interannual variability of JES SSTA have been investigated using correlation analysis between the *n*-th mode JES SSTA and background SLPA, SATA, SSTA, and four climate indices: AOI, NPI, MEI, and WPI. The first (second) mode SSTA is the most correlated with NPI (AOI) leading by 3~6 months (1~1.5 years) among four climate indices. The correlation to the background SLPA and SATA demonstrates that the first mode SSTA is mainly controlled by adjacent atmospheric systems, i.e., the Aleutian Low, the North Pacific High, the Siberian High, and the East Asian jet stream. In particular, the East Asian jet stream is dynamically coupled to the surface lows and highs, so its influence on the first mode SSTA is significant. The correlation of the first mode SSTA to the background SSTA closely resembles that to the background SATA, and the corresponding positive correlation zonal belt is indicative of the Polar Front in the North Pacific where the intensive ocean-atmosphere interaction occurs. This suggests that the oceanic and atmospheric factors influencing the first mode SSTA are strongly coupled. The second mode SSTA is associated with the Arctic Oscillation signal transferring from the high latitudes (north of 40°N) to the low latitudes, inferred from the strong correlation to background SLPA in the high (low) latitudes at negative (positive) lags. This is also supported by the correlation to the background SATA, suggesting that the Arctic Oscillation can affect the second mode SSTA in the northeastern JES via the northern boundary of the Siberian High. Moreover, the strong correlation in the tropical to subtropical western Pacific of the background SATA and SSTA implies that cooling (warming) in the Subtropical Gyre is accompanied by cooling (warming) in the second mode of the southwestern (northeastern) JES.

Acknowledgements

This research was supported by the Post-doctoral Fellowship Program of Korea Science and Engineering Foundation (KOSEF), Office of Naval Research, Naval Oceanographic Office, and Naval Postgraduate School.

References

Alexander, A. M., I. Bladé, M. Newman, J. R. Lanzante and N.-C. Lau (2002): Atmospheric bridge: the influence of ENSO teleconnections on air-sea Interaction over the global oceans. *J. Climate*, **15**(16), 2205–2231.

Barnston, A. G. and R. E. Livezey (1987): Classification, seasonality and persistence of low-frequency atmospheric circulation patterns. *Mon. Wea. Rev.*, **115**, 1083–1126.

Beckers, J. M. and M. Rixen (2003): EOF calculations and data filling from incomplete oceanographic datasets. *J. Atmos. Ocean. Technol.*, **20**, 1839–1856.

Chu, P. C. and C. L. Fang (2003): Observed Rossby waves in the South China Sea from satellite altimetry data. *Proc. SPIE on Remote Sensing of the Ocean and Sea Ice*, 142–149.

Chu, P. C., H. C. Tseng, C. P. Chang and J. M. Chen (1997): South China Sea warm pool detected in spring from the Navy's Master Oceanographic Observational Data Set (MOODS). *J. Geophys. Res.*, **102**(C7), 15,761–15,771.

Chu, P. C., Y. C. Chen and S. H. Lu (1998): Temporal and spatial variabilities of Japan Sea surface temperature and atmospheric forcings. *J. Oceanogr.*, **54**(3), 273–384.

Chu, P. C., J. Lan and C. W. Fan (2001a): Japan Sea circulation and thermohaline structure, Part 1, Climatology. *J. Phys. Oceanogr.*, **31**, 244–271.

Chu, P. C., J. Lan and C. W. Fan (2001b): Japan Sea circulation and thermohaline structure, Part 2, A variational P-vector method. *J. Phys. Oceanogr.*, **31**, 2886–2902.

Chu, P. C., G. H. Wang and Y. C. Chen (2002): Japan Sea circulation and thermohaline structure, Part 3, Autocorrelation functions. *J. Phys. Oceanogr.*, **32**, 3596–3615.

CLIVAR (2003): A multi-millennia perspective on drought and implications for the future. *Proceedings of CLIVAR/PAGES/IPCC Workshop*, 33 pp.

Gong, D.-Y. and C.-H. Ho (2002): Can the Arctic Oscillation impact the East Asian summer monsoon? *CLIVAR Exchanges*, **7**(1), 18–20.

Gong, D.-Y. and C.-H. Ho (2003): Arctic Oscillation signals in the East Asian summer monsoon. *J. Geophys. Res.*, **108**(D2), 4066, doi:10.1029/2002JD002193.

Gong, D.-Y. and S.-W. Wang (2003): Influence of Arctic Oscillation on winter climate over China. *J. of Geographical Science*, **13**(2), 208–216.

Gong, D.-Y., S.-W. Wang and J.-H. Zhu (2001): East Asian winter monsoon and Arctic Oscillation. *Geophys. Res. Lett.*, **28**(10), 2073–2076.

Hase, H., J.-H. Yoon and W. Koterayama (1999): The current structure of the Tsushima Warm Current along the Japanese Coast. *J. Oceanogr.*, **55**(2), 217–235.

Hirose, N. and A. G. Ostrovskii (2000): Quasi-biennial variability in the Japan Sea. *J. Geophys. Res.*, **105**(C6), 14011–14027.

Hong, C.-H., K.-D. Cho and H.-J. Kim (2001): The relation-

ship between ENSO events and sea surface temperature in the East (Japan) Sea. *Prog. Oceanogr.*, **49**(1), 21–40.

Jhun, J.-G. and E.-J. Lee (2004): A new east Asian winter monsoon index and associated characteristics of the winter monsoon. *J. Climate*, **17**(4), 711–726.

Lau, K.-M., K.-M. Kim and S. Yang (2000): Dynamical and boundary forcing characteristics of regional components of the Asian Summer Monsoon. *J. Climate*, **13**(14), 2461–2482.

Lin, H., J. Derome, R. J. Greatbatch, K. A. Peterson and J. Lu (2002): Tropical Links of the Arctic Oscillation. *Geophys. Res. Lett.*, **29**(20), 1943, doi:10.1029/2002GL015822.

Lin, Z. and R. Lu (2005): Interannual Meridional Displacement of the East Asian upper-tropospheric jet stream in summer. *Advanced in Atmospheric Science*, **22**(2), 199–211.

McPhaden, M. J. (2002): TAO/TRITON tracks Pacific Ocean warming in early 2002. *CLIVAR Exchanges*, **24**, 7–9.

Minobe, S. (2002): Interannual to interdecadal changes in the Bering Sea and concurrent 1998/1999 changes over the North Pacific. *Prog. Oceanogr.*, **55**, 45–65.

Minobe, S., A. Sako and M. Nakamura (2004): Interannual to interdecadal variability in the Japan Sea based on a new gridded upper water temperature dataset. *J. Phys. Oceanogr.*, **34**, 2382–2397.

Morimoto, A. and T. Yanagi (2001): Variability of sea surface circulation in the Japan Sea. *J. Oceanogr.*, **57**(1), 1–13.

Morimoto, A., T. Yanagi and A. Kaneko (2000): Eddy field in the Japan Sea derived from satellite altimetric data. *J. Oceanogr.*, **56**(4), 449–462.

Niebauer, H. J., N. A. Bond, L. P. Yakunin and V. V. Plotnikov (1999): An update on the climatology and sea ice of the Bering Sea. p. 29–60. In *Dynamics of the Bering Sea: A Summary of Physical, Chemical, and Biological Characteristics, and a Synopsis of Research on the Bering Sea*, ed. by T. R. Loughlin and K. Ohtani, Univ. of Alaska Sea Grant.

Nonaka, M. and S.-P. Xie (2003): Covariations of sea surface temperature and wind over the Kuroshio and its extension: evidence for ocean-to-atmosphere feedback. *J. Climate*, **16**(9), 1404–1413.

Oelke, C., T. Zhang and M. C. Serreze (2004): Modeling evidence for recent warming of the Arctic soil thermal regime. *Geophys. Res. Lett.*, **31**(7), L07208, doi:10.1029/2003GL019300.

Overland, J. E. and R. W. Preisendorfer (1982): A significance test for principal components appied to cyclone climatology. *Mon. Wea. Rev.*, **110**(1), 1–4.

Park, K. A. (1996): Spatial and temporal variability of sea surface temperature and sea level anomaly in the East Sea using satellite data (NOAA/AVHRR, TOPEX/ALT). Ph.D. Dissertation, Seoul National University, Korea, 294 pp.

Park, W.-S. and I.-S. Oh (2000): Interannual and interdecadal variations of sea surface temperature in the East Asian Marginal Sea. *Prog. Oceanogr.*, **47**, 191–204.

Ponomarev, V., O. Trusenkova, S. Trousenkov, D. Kaplunenko, E. Ustinova and A. Polyakova (1999): The ENSO signal in the Northwest Pacific. p. 13–30. In *Proceedings of the 1998 Science Board Symposium on the Impacts of the 1997/98 El Niño Event on the North Pacific Ocean and Its Marginal Seas*, Pacific Oceanological Institute Russian Academy of Sciences.

Schwing, F. B., T. Murphree, L. deWitt and P. M. Green (2002): The evolution of oceanic and atmospheric anomalies in the Northeast Pacific during the El Niño and La Niña events of 1995–2000. *Prog. Oceanogr.*, **54**, 459–491.

Shriver, J. E., M. A. Johnson and J. J. O'Brien (1991): Analysis of remotely forced oceanic Rossby waves off California. *J. Geophys. Res.*, **96**(C1), 749–757.

Thompson, D. W. J. and J. M. Wallace (1998): The Arctic Oscillation signature in the wintertime geopotential height and temperature fields. *Geophys. Res. Lett.*, **25**(9), 1297–1300.

Thompson, D. W. J. and J. M. Wallace (2001): Regional climate impacts of the northern hemisphere annular mode and associated climate trends. *Science*, **293**, 85–89.

Trenberth, K. E. and J. W. Hurrell (1994): Decadal atmosphere-ocean variations in the Pacific. *Climate Dynamics*, **9**, 303–319.

Trousenkov, S. T., O. O. Trusenkova, V. I. Ponomarev and H. Ishida (2001): Complex EOF patterns of the Northwest Pacific SST anomalies. p. 145–149. In *Proceedings of CREAMS'2000, Oceanography of the Japan Sea*.

Vazquez, J., K. Perry and K. Kilpatrick (1998): NOAA/NASA AVHRR Oceans Pathfinder Sea Surface Temperature Data Set User's Reference Manual Version 4.0. JPL Publication D-14070 (available at http://www.nodc.noaa.gov/woceV2/disk13/avhrr/docs/usr_gde4_0_toc.htm).

Venegas, S. A. (2001): Statistical Methods for Signal Detection in Climate. Danish Center for Earth System Science Report #2, 96 pp.

Venegas, S. A., L. A. Mysak and D. N. Straub (1998): An interdecadal climate cycle in the South Atlantic and its links to other ocean basins. *J. Geophys. Res.*, **103**(C11), 24,723–24,736.

Wang, B., R. Wu and X. H. Fu (2000): Pacific-East Asian teleconnection: How does ENSO affect East Asian climate? *J. Climate*, **13**(9), 1517–1536.

Wang, C., R. H. Weisberg and J. I. Virmani (1999): Western Pacific interannual variability associated with El Niño-Southern Oscillation. *J. Geophys. Res.*, **104**(C3), 5131–5149.

Wilks, D. S. (1995): *Statistical Methods in the Atmospheric Sciences*. Academic Press, San Diego, 467 pp.

Wolter, K. and M. S. Timlin (1993): Monitoring ENSO in COADS with a seasonally adjusted principal component index. *Proc. of the 17th Climate Diagnostics Workshop*, 52–57.

Wolter, K. and M. S. Timlin (1998): Measuring the strength of ENSO—How does 1997/98 rank? *Weather*, **53**, 315–324.

Wu, B. and J. Wang (2002): Winter Arctic Oscillation, Siberian High and East Asian Winter Monsoon. *Geophys. Res. Lett.*, **29**(19), 1897, doi:10.1029/2002GL015373.

Yang, S., K.-M. Lau and K.-M. Kim (2002): Variations of the East Asian Jet Stream and Asian-Pacific-American winter climate anomalies. *J. Climate*, **15**(3), 306–325.

Yang, S., K.-M. Lau, S.-H. Yoo, J. L. Kinter and K. Miyakoda (2004): Upstream subtropical signals preceding the Asian Summer monsoon circulation. *J. Climate*, **17**(21), 4213–4229.

Yoo, S.-H., C.-H. Ho, S. Yang, H.-J. Choi and J.-G. Jhun (2004): Influences of tropical-western and extratropical Pacific SSTs on the East and Southeast Asian climate in the summers of 1993–94. *J. Climate*, **17**(13), 2673–2687.